Oxid Met (2013) 79:405–427
DOI 10.1007/s11085-013-9364-4

ORIGINAL PAPER

Slow Transition from Protective to Breakaway Oxidation of Haynes 214 Foil at High Temperature

D. J. Young · A. Chyrkin · J. He · D. Grüner · W. J. Quadakkers

Received: 7 November 2012 / Revised: 15 January 2013 / Published online: 26 January 2013

Abstract The oxidation behaviour of thin sheet specimens of the alumina forming nickel base alloy 214 in the temperature range 1,100–1,200 °C is described. Rapid transient oxidation produces a spinel oxide layer which then stops growing, as a protective alumina layer forms beneath. The slow growth of this alumina ceases when the alloy aluminium content is exhausted. Subsequent formation of an innermost chromia layer signals an increase in oxygen activity at the scale-alloy interface. The abnormally slow growth of this layer extends the alloy lifetime. Examination of individual layer growth processes revealed a complex time dependence of spinel composition as a result of Cr evaporation, and dissolution of alumina in the innermost chromia.

Keywords Nickel base alloy · Breakaway oxidation · Alloy 214 · Alumina · Cr-evaporation · Transient spinel

Introduction

Nickel base high temperature alloys are commonly used as construction materials for components operating at high temperatures in oxidizing environments. For their protection against oxidation attack, most of these alloys rely on the formation of a slowly growing chromium oxide layer on the alloy surface during high temperature

J. He was formerly with Forschungszentrum Jülich GmbH.

D. J. Young
School of Materials Science and Engineering, The University of New South Wales, Sydney, NSW 2052, Australia

A. Chyrkin (✉) · J. He · D. Grüner · W. J. Quadakkers
Forschungszentrum Jülich GmbH, IEK-2, 52425 Julich, Germany
e-mail: a.chyrkin@fz-juelich.de

service. From the viewpoint of oxidation resistance, the maximum operating temperature of such alloys is limited to approximately 1,000 °C, the exact temperature depending on the actual component design, service environment, required lifetime, etc. [1]. Beyond that temperature, rapid oxidation attack may occur as a result of enhanced growth rates of the chromia surface scales in combination with the formation of volatile $CrO_3(g)$ and $CrO_2(OH)_2(g)$, the latter being especially important in gases containing substantial amounts of water vapour [2–5].

Far better resistance against oxidation attack can be obtained from surface scales consisting mainly of aluminium oxide. There are a number of alumina forming nickel base materials which form such very slowly growing surface scales. Alloys of the NiCrAlY or NiCoCrAlY type, which typically contain e.g. 15–25 mass% Cr and 6–12 % Al, are, however, mainly used as coatings, e.g. on nickel base superalloy components in aero engines and industrial gas turbines [6, 7]. They are not suitable as construction materials mainly due to their inherent brittleness at low temperatures and the lack of formability into semi finished products such as sheets, bars and tubes. Some of the newer types of nickel base superalloys such as CXMSX-4 or Rene N5 [8, 9] may to a first approximation also be considered as alumina forming materials. However, these materials can not be processed as wrought alloys, mainly due to their high concentrations of γ' stabilizing alloying elements such as Al, Ti and/or Ta.

Only a few wrought nickel base alloys are commercially available with aluminium levels sufficient to form alumina base surface scales during high temperature exposure. Examples of such materials are Nicrofer 6025 HT, Haynes 224 and Haynes 214 [10, 11], the last having a higher aluminium content than the others. Compared to alumina forming FeCrAl type alloys, the nickel base materials possess substantially higher creep strength, which makes them suitable as construction materials for thin walled components such as heat exchangers, honeycomb structures and catalyst carriers [12, 13].

In spite of their superior oxidation resistance, the lifetime of components manufactured from wrought alumina forming alloys is limited by oxidation during long term service at temperatures at and above about 1,100 °C [14, 15]. The reason is that during high temperature exposure, aluminium is depleted in the alloy matrix due to its selective oxidation into the protective scale. The depletion can be made worse by repeated scale spallation and re-growth induced by thermal cycling. If the remaining aluminium content is decreased beneath a critical concentration, the alloy can no longer re-form the protective scale, and breakaway oxidation—the formation of rapidly growing base metal oxides—results [11, 16]. The time at which this breakaway oxidation commences cannot be predicted from the results of commonly available non-destructive tests. Prediction requires a comparison of the scale growth rate and spallation with the available Al-reservoir in the respective component [14, 15, 17].

In the present paper, the oxidation induced lifetime of the alumina forming nickel base wrought alloy 214 has been investigated in the temperature range 1,100–1,200 °C. A number of oxidation results are available in the literature for this material [10, 18]. In a few cases breakaway times were estimated and compared

with those obtained for FeCrAl type materials [11]. However, as far as is known to the authors, detailed microstructural studies of the surface scales, the kinetics of aluminium depletion and the mechanisms of breakaway are not available. For this reason, the emphasis of the present study is on evaluation of the oxidation kinetics, oxide scale composition and morphology, and changes in bulk alloy composition with time in the temperature range 1,100–1,200 °C. The studies concentrate on thin sections, for which breakaway is expected to occur before substantial oxide scale spallation [14, 19].

Experimental Procedures

Oxidation test specimens measuring 12 × 12 × 0.13 mm were cut from a rolled tape of Haynes® 214 alloy supplied by Haynes International, Inc. The measured chemical composition of the alloy is given in Table 1. According to the datasheet of Haynes® 214, the alloy contains reactive elements Zr and Y up to 0.1 and 0.01 wt%, respectively. After cleaning and degreasing, the specimens were oxidized discontinuously in laboratory air at 1,100, 1,150 and 1,200 °C up to maximum exposure times of 1000, 1200 and 600 h, respectively. The specimens were moved into the hot furnace so that the time to reach the respective exposure temperature was approximately 2 min. Oxidized specimens were weighed, after cooling to room temperature, after 100, 300, and 1,000 h at 1,100 °C, every 200 h at 1,150 °C and every 100 h at 1,200 °C. Thus a single specimen was withdrawn from the experiment after each cooling step. Continuous weight uptake kinetics were observed thermogravimetrically with a SETARAM Thermobalance for the first 72 h of reaction in air, at 1,100 and 1,200 °C. The specimen heating rate in theses tests was 90 K per minute.

The oxidized specimens were electroplated with nickel and metallographically sectioned. The resulting cross-sections were characterized by optical metallography and scanning electron microscopy (SEM) with energy dispersive X-ray analysis (EDX) and wavelength dispersive X-ray analysis (WDX).

For a more detailed investigation of the phase composition of the oxide scales formed on the alloy surface, the 1,150 °C specimens were analyzed by X-ray diffraction (XRD) using Cu K_α radiation in the D4 ENDEAVOR set-up from BRUKER AXS.

Selected specimens were analyzed by secondary neutral mass spectrometry (SNMS). The measured depth profiles were quantified using a procedure similar to that described in Refs. [20, 21].

Table 1 Chemical composition in weight and atomic percent of alloy Haynes 214 analyzed by ICP-OES

Element	Ni	Cr	Al	Fe	Mn	Si
wt%	75.0	16.5	4.5	3.57	0.17	0.26
at%	69.5	17.3	9.07	3.46	0.17	0.5

Results and Discussion

Protective Scaling of Alloy 214

Weight gain kinetics are shown in Fig. 1 as both continuous TGA measurements and long term interrupted exposure results. In the latter, each point represents a separate sample. Initially, protective behaviour is observed at all test temperatures (Fig. 1a). At the lowest temperature, protective scaling continued up to the longest time observed (1,000 h). At 1,200 °C, breakaway kinetics were clearly evident, and at 1,150 °C reaction kinetics were intermediate in character.

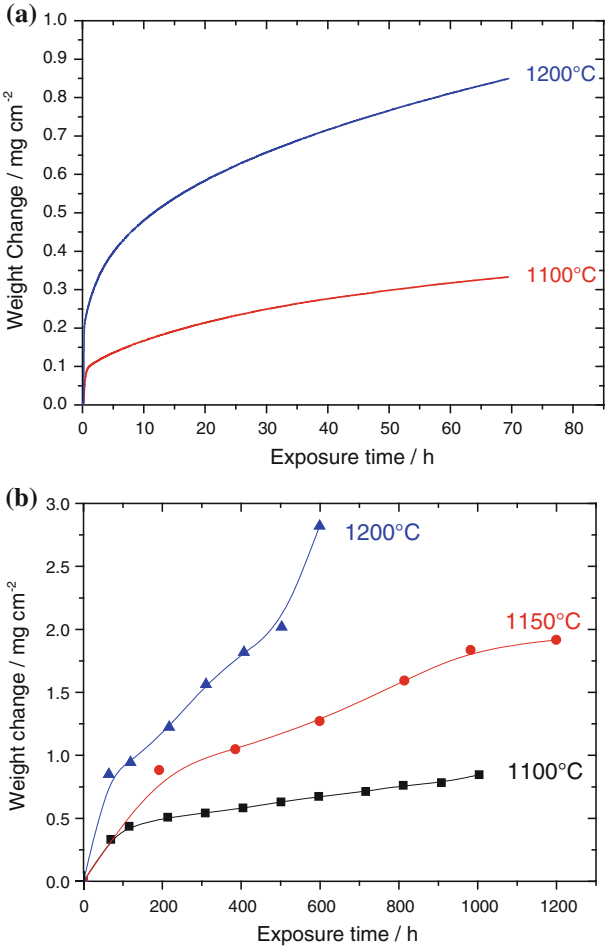

Fig. 1 Weight change for Haynes 214 alloy between 1,100 and 1,200 °C during isothermal oxidation in laboratory air: **a** TG-curves; **b** discontinuous oxidation. The first data points in the 1,100 and 1,200 °C curves were taken from (**a**)

A protective scale grown for 100 h at 1,200 °C is shown in cross-section in Fig. 2. The accompanying EDS results confirm that the scale consists of an outer layer of Ni/Al-spinel containing minor amounts of Cr and an inner layer of Al_2O_3, in agreement with observations in Refs. [10, 22]. This is the expected form of a protective scale on a nickel base, alumina forming alloy [23]. The question of interest concerns the way in which this microstructure evolves with time.

Individual sublayer thicknesses at 1,100 °C are seen in Fig. 3a to reflect slow growth of the alumina layer, but the thickness of the spinel layer does not increase with time. Clearly, neither nickel nor chromium diffuses through the inner alumina layer at this temperature in the given time period. The presence of the spinel layer must therefore result from an initial period of transient oxidation in which nickel, chromium and aluminum reacted [24–28]. Examination of the continuous TGA curve in Fig. 1a reveals a short initial period of rapid reaction, during which nickel and chromium presumably oxidized. As shown in Fig. 4, the instantaneous apparent

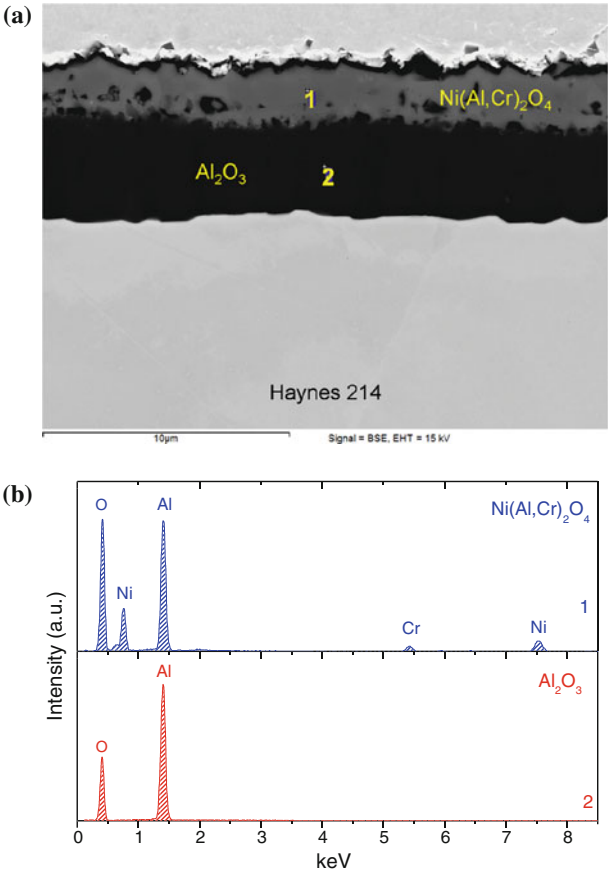

Fig. 2 Protective scale formed on Haynes 214 after 100 h air oxidation at 1,200 °C (**a**) and EDX spectra (**b**) of points indicated in (**a**)

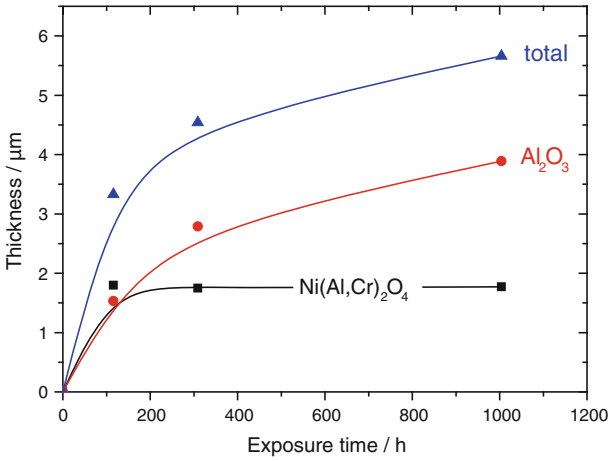

Fig. 3 Thickening kinetics of individual oxide layers formed on Haynes 214 during oxidation in air at 1,100° C

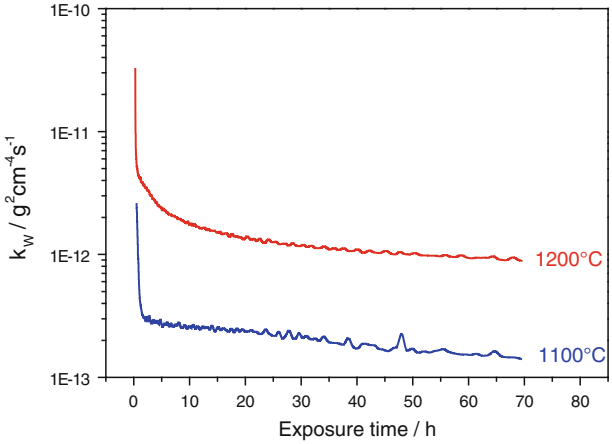

Fig. 4 Measured instantaneous apparent parabolic rate constant as function of oxidation time during isothermal oxidation (compare with Fig. 1)

parabolic rate constant, calculated from the TG-curves, drops abruptly within the first few hours of exposure, by an order of magnitude.

For simplicity we assume in the following that the outer spinel layer is pure $NiAl_2O_4$. Once a continuous Al_2O_3 layer was established, and the supply of nickel to the outer layer was blocked, then any NiO formed during transient oxidation would become unstable with respect to spinel. The reaction

$$NiO(s) + Al_2O_3(s) = NiAl_2O_4(s) \quad (1)$$

for which $\Delta G^\circ = -6265 - 9.7\ T\ J\ mol^{-1}$ [29, 30] is favored, leading to formation of the spinel layer.

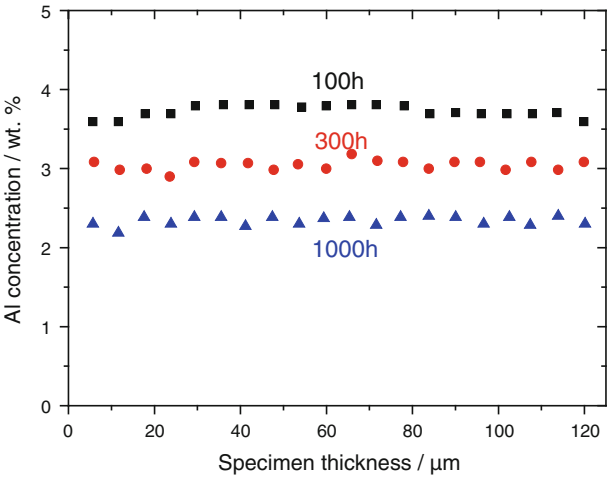

Fig. 5 EDX concentration profiles of Al in bulk alloy after air oxidation at 1,100 °C

Continued growth of the alumina layer depletes aluminum from the thin alloy foil. Figure 5 shows the Al concentration in the bulk alloy after exposure at 1,100 °C for 1,000 h. The result clearly shows that hardly any gradient in Al concentration exists, i.e. the Al profiles are virtually flat, especially after longer times. These flat profiles were also found after oxidation at higher temperatures, as will be illustrated later. Average foil compositions shown in Fig. 6a reflect a gradual decrease in Al concentration corresponding to slow alumina scaling.

Transition from Alumina to Chromia Formation

At 1,150 °C, oxidation is considerably faster (Fig. 1), and leads to complete consumption of the alloy aluminum content (Fig. 6b). All aluminium was removed from the alloy foil after about 800 h of reaction, and alumina scaling ceased. At 1,200 °C aluminium is completely depleted in half the time, approximately 400 h (Fig. 6c). As aluminium is no longer present in the alloy, chromium is expected to oxidize. This effect is indeed observed and is most pronounced at the highest oxidation temperature, resulting in a decrease in remnant alloy chromium concentration after 400 h (Fig. 6c).

Concentration profiles measured across the entire foil thickness at 1,200 °C, and shown in Fig. 7a, are progressively reduced to lower levels as Al is drained from the alloy. Because of the low oxidation rate in combination with a relatively high aluminum diffusion coefficient in alloy 214, ($D_{Al} = 1.6 \times 10^{-9}$ cm^2 s^{-1} at 1,200 °C) [31–33], the concentration profiles remain flat. Chromium concentrations within the alloy are little changed in the first 400 h of reaction at 1,200 °C, but are progressively lowered with the further passage of time. As seen in Fig. 7b, the chromium concentration profiles remain flat, indicating that the rate of chromium consumption is slow compared to the rate of alloy diffusion.

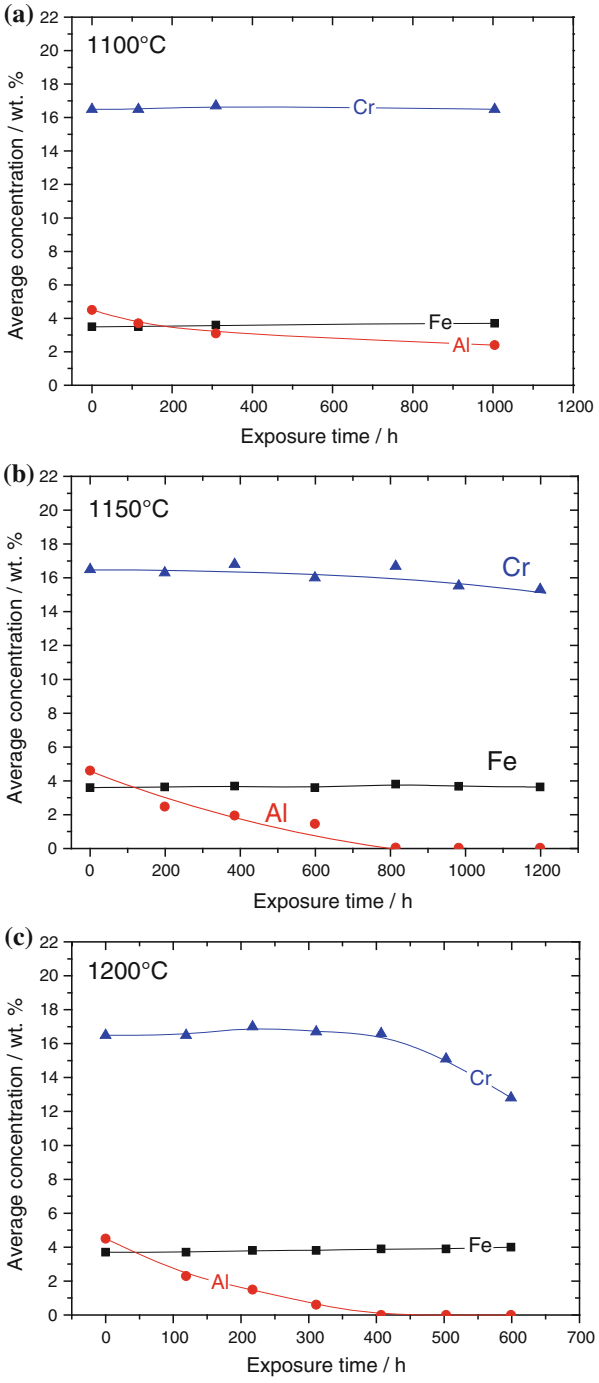

Fig. 6 Average Al and Cr concentrations in bulk alloy as function of time at various oxidation temperatures (measured by EDS)

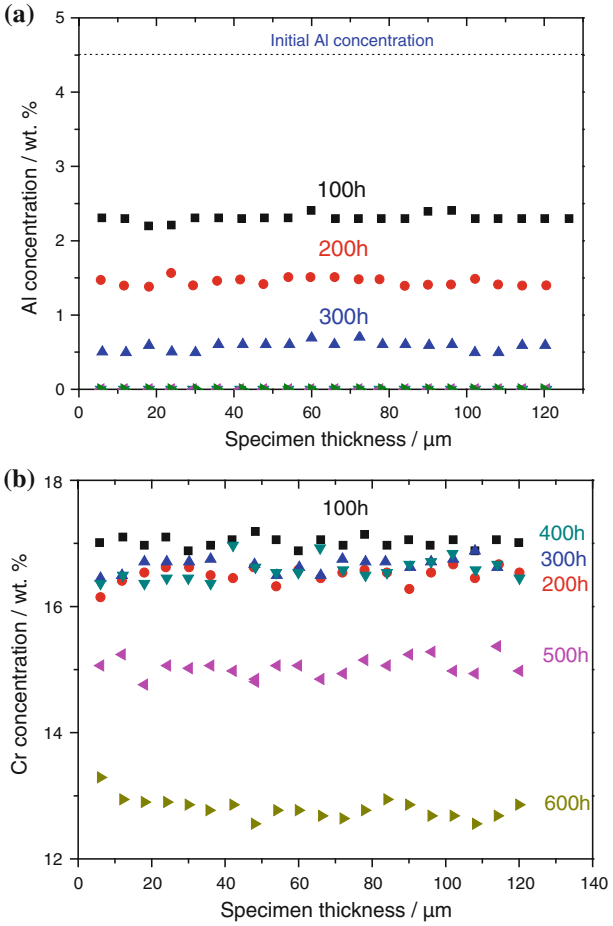

Fig. 7 EDX concentration profiles of Al (**a**) and Cr (**b**) in bulk alloy during oxidation at 1,200 °C

The evolution of scale microstructure at 1,150 °C is seen in Fig. 8 to be more complex than at 1,100 °C. After about 800 h, a new oxide layer develops at the scale-alloy interface, and grows thicker with additional reaction time (Fig. 9). Analysis by EDS of this layer after 1,200 h reaction showed it to be rich in both chromium and aluminum. Clearly, chromium derived from the alloy substrate, but aluminum could come only from the alumina layer in the scale.

The formation of a chromia-containing layer between the alumina and the alloy after 800 h oxidation at 1,150 °C was confirmed by XRD analysis. Because the alumina and spinel layers are thin and relatively transparent to X-rays, conventional XRD analysis of oxide scales produced diffraction patterns containing reflections from the underlying alloy matrix phase. Any new oxide layer developed at the alumina-alloy interface should therefore be detected by XRD, once enough of it had formed. As seen in Fig. 10, diffraction from Cr_2O_3 is distinguished from Al_2O_3 in the 2θ range of 33–36°, and is evident in samples oxidized for 1,000 and 1,200 h at

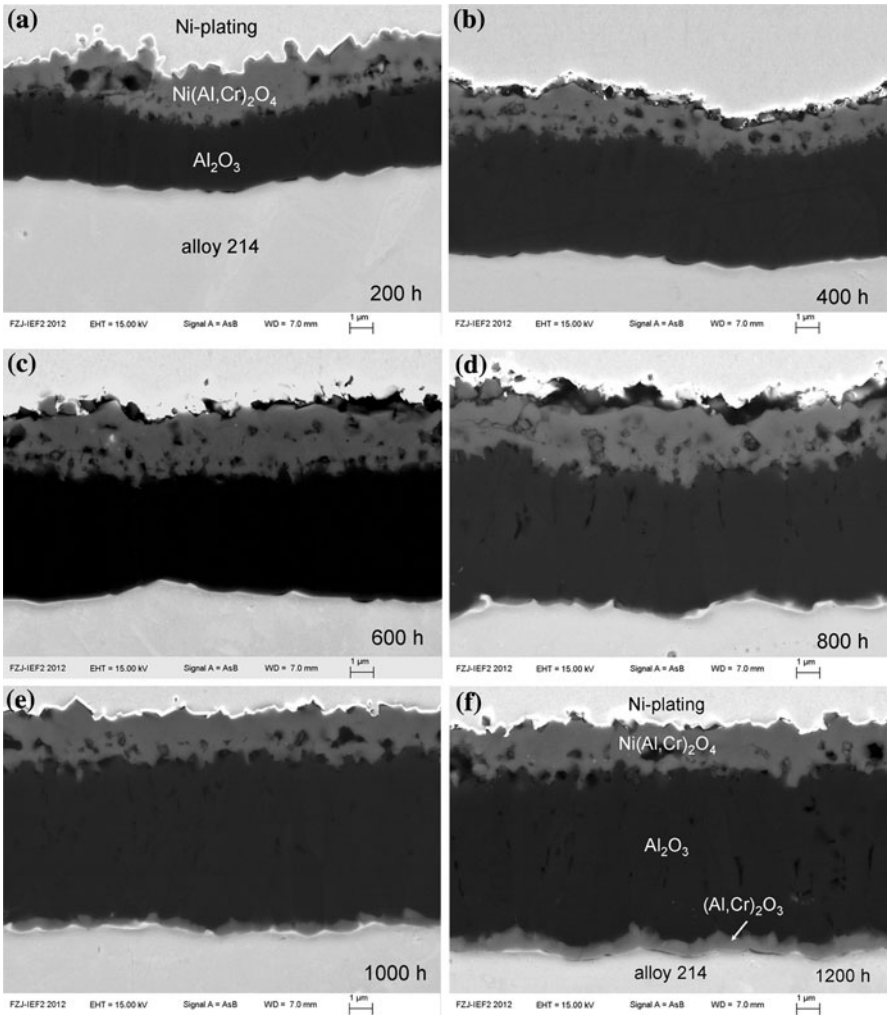

Fig. 8 Oxide scale morphology evolution during air exposure at 1,150 °C (200–1,200 h)

1,150 °C, but not for shorter times. The strongest reflection (104) from Al_2O_3 (corundum, PDF File No. 46-1212) appears in the XRD pattern (copper K_α wavelength 1.5419 Å) at 35.2° which is seen in Fig. 10. The new peak observed after 1000 h oxidation is at 34.0°, although the (104) peak of Cr_2O_3 (Eskolaite, PDF File No. 38-1476) is expected at 33.6°. As was shown by Bondioli et al. [34], Cr_2O_3-Al_2O_3 solid solutions prepared by co-precipitation from aqueous solution with subsequent heat treatment at 1,200–1,500 °C exhibit a concentration dependence of the unit cell parameters *a* and *c*, increasing from 4.758 and 12.991 Å for pure alumina to 4.958 and 13.594 Å for pure chromia. It is thus concluded that the newly developed, chromium-rich layer is in fact at least partly made up of chromia containing dissolved Al. Oxides marked on the cross-sections of Fig. 8 reflect this identification.

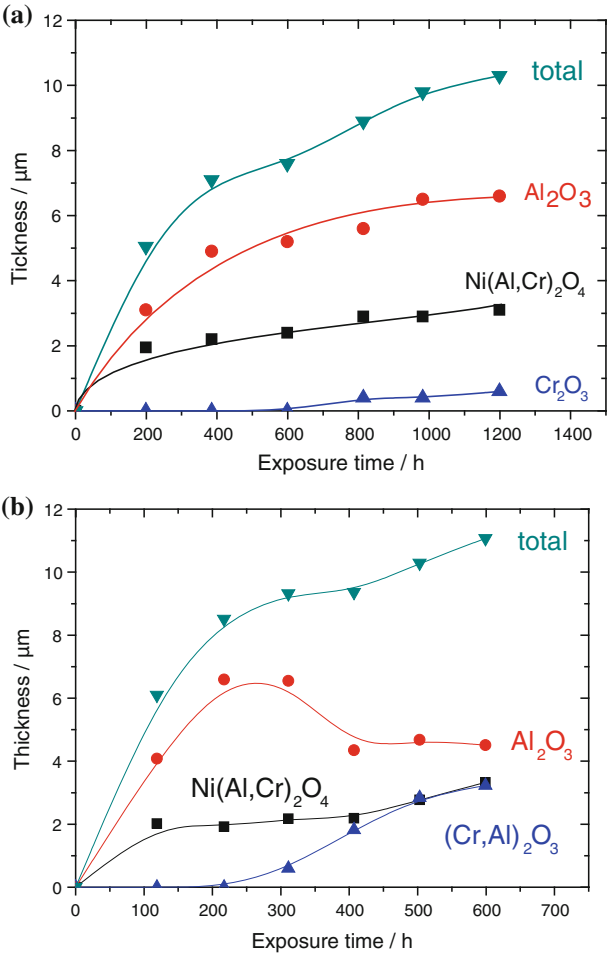

Fig. 9 Thickening kinetics of individual oxide layers formed on Haynes 214 during air exposure at 1,150 (**a**) and 1,200 °C (**b**)

Elemental profiles across the oxide scale obtained by SNMS after oxidation at 1,150 °C are shown in Fig. 11. During the protective oxidation stage, after 200 h (Fig. 8a), only two oxide sublayers can be distinguished: outer Ni-rich spinel and inner alumina which serves as a barrier for base alloy elements Ni, Cr and Fe. The spinel contains a time dependent concentration of chromium as is discussed later. After aluminum is completely consumed and chromia starts to grow at the scale-alloy interface, the alumina layer, no longer in direct contact with the substrate alloy, becomes permeable to nickel and chromium (Fig. 11b). The Ni and Cr concentrations in the middle of the alumina sublayer increase up to 1–2 at%. A gradual decrease in aluminum concentration towards the alloy substrate indicated absorption of Al by the growing chromia sublayer.

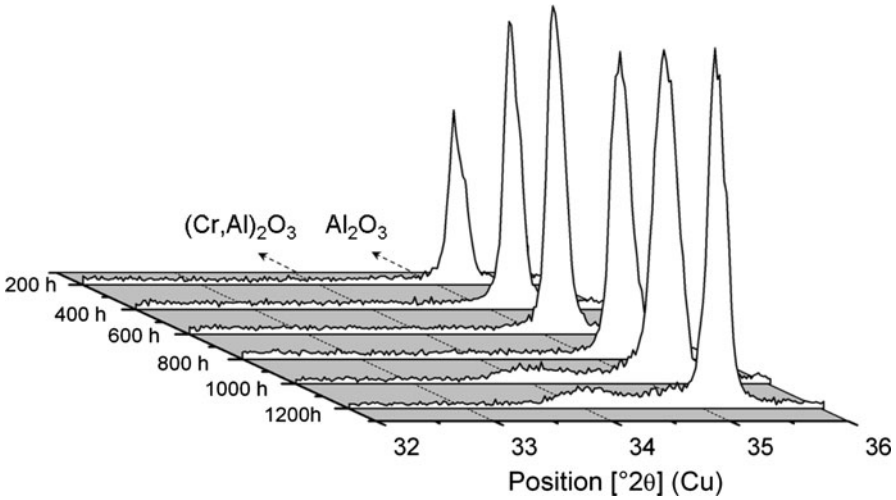

Fig. 10 XRD patterns of oxide scales formed on Haynes 214 during air exposure at 1,150 °C. Weak reflexes at $2\theta = 34°$ indicate formation of $(Cr,Al)_2O_3$ solid solution after 800 h of oxidation

The processes described for the 1,150 °C oxidation are even more pronounced at 1,200 °C. The onset of subscale chromia formation is seen in Fig. 12a after only 300 h of oxidation. This chromia interacted with the overlying alumina layer, resulting in a thinning of the Al_2O_3, as seen qualitatively in Fig. 12. Average layer thickness measurements in Fig. 9b show that both the underlying chromia and the outermost spinel grew at the expense of the prior alumina.

EDX spectra of individual oxide layers of the scale grown after the longest exposure time of 600 h at 1,200 °C are shown in Fig. 13. The subscale chromia was found to contain approximately 10 at% Al (see Table 2). Strong interdiffusion of Al and Cr in the innermost oxide layer is illustrated by the WDX line scan in Fig. 14.

The pseudo steady-state situation in which chromia forms at the alumina-alloy interface whilst the prior alumina is consumed is important. This stage of reaction is still slow (Fig. 1b), and thus represents an effective extension of alloy life beyond the point where its aluminum content is exhausted.

Chromia formation beneath an external alumina scale has been previously observed during breakaway studies of FeCrAl-base alloys [15, 35–37]. At temperatures in the range 1,100–1,200 °C, exhaustion of the aluminum reservoir in thick specimens of a few mm resulted in formation of rapidly growing Fe-rich oxides. However, in the case of thin specimens, e.g. 50–100 μm thick, this event was preceded by a "pseudo protective" period in which subscale chromia formation occurred. Evans and Taylor [38] studied breakaway processes in plasma sprayed Ni(Co)CrAlY coatings at 1,100 °C. In isolated particles, the initially formed alumina layer was destroyed by breakaway oxidation, in which the first stage of the process was subscale chromia formation. However, as far as is known to the authors, the process of alumina dissolution in the subscale chromia has not yet been described.

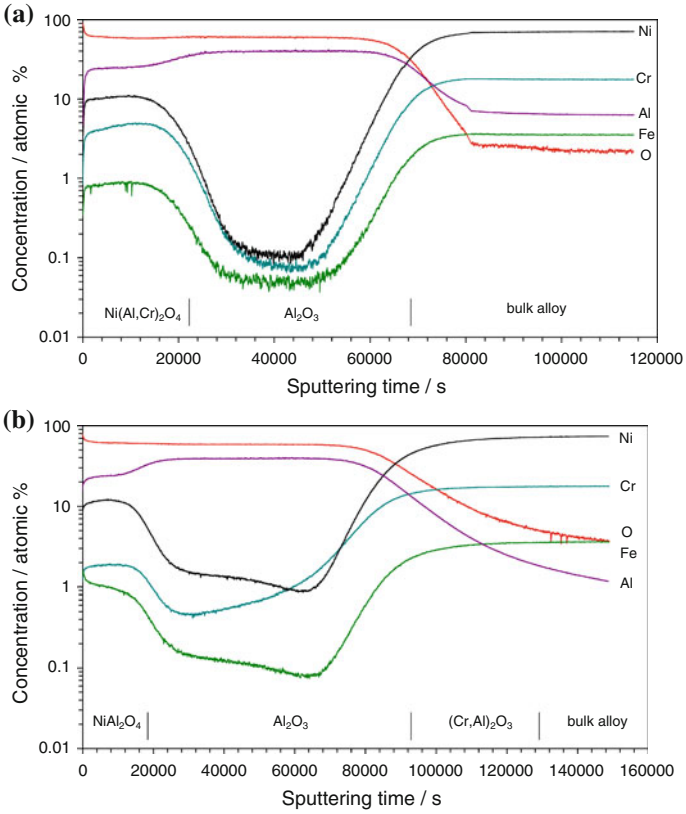

Fig. 11 SNMS depth profiles across oxide scale grown on Haynes 214 after 200 (**a**) and 1,200 h (**b**) of air exposure at 1,150 °C

Chromia scale formation is not normally regarded as a satisfactory strategy for alloy protection at 1,200 °C. This is because scaling is relatively rapid, leading to significant alloy surface recession. Chromia scaling rates were reviewed by Caplan and Sproule [39] and described in terms of parabolic weight uptake kinetics

$$\left(\frac{\Delta W}{A}\right)^2 = 2k_w t \tag{2}$$

where $\Delta W/A$ is the weight uptake per unit area in time, t, and k_w the rate constant. At 1,200 °C, a wide range of k_w values are reported, but most fell within the band 10^{-11}–10^{-9} g^2 cm^{-4} s^{-1} [39]. If these values were applied to the present case (Fig. 9) where Cr-rich oxide grew for approximately 300 h, a layer thickness of 20–200 μm would be predicted, far greater than the measured average value of approximately 3 μm (Fig. 12d). The reason for this difference is, of course, the presence of a continuous layer of alumina above the inner chromia layer. Thus the oxygen potential at the outer interface of the chromia scale is decreased by the

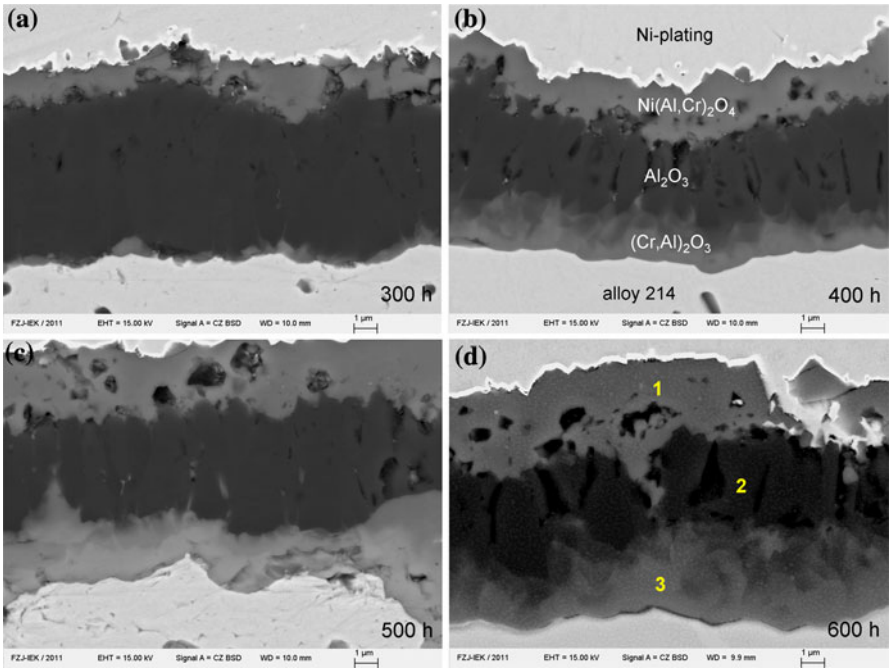

Fig. 12 Oxide scale morphology evolution during air exposure (300–600 h) at 1,200 °C

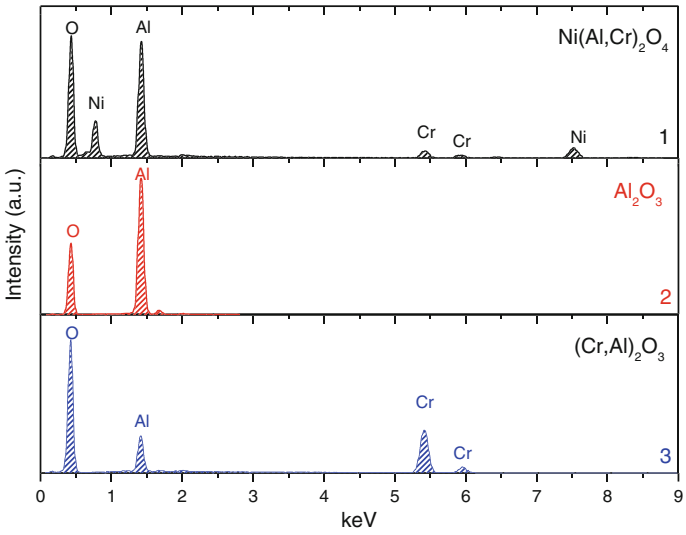

Fig. 13 EDS spectra of oxide layers formed on Haynes 214 specimen after 600 h air exposure at 1,200 °C shown in Fig. 12d

Table 2 Chemical composition (in at%) of oxide layers in Fig. 12d measured by EDX

Spectrum	O	Al	Cr	Ni	Mn	Fe
1	56.5	25.6	3.5	12.2	1.3	0.9
2	60.5	39.5	–	–	–	–
3	60.2	10.2	28.9	0.7	–	–

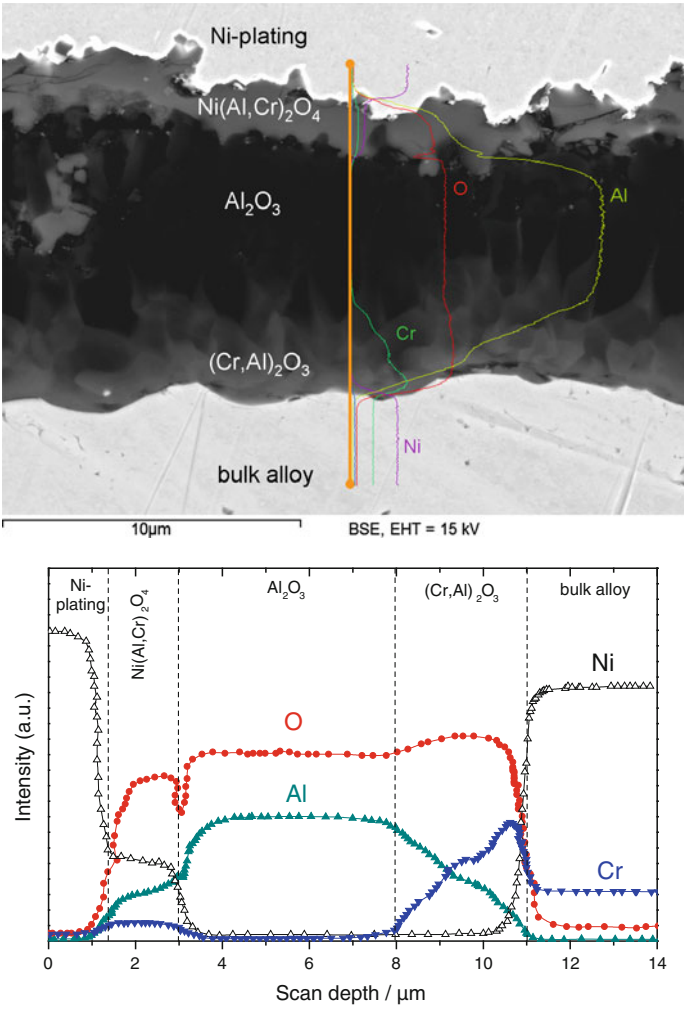

Fig. 14 WDX line scan across oxide scale formed on Haynes 214 alloy after 500 h air exposure at 1,200 °C

alumina layer, and the driving force for chromia growth is decreased. An additional benefit provided by the outer oxide (alumina and spinel) is in preventing chromium volatilization via reaction

$$Cr_2O_3(s) + \frac{3}{2}O_2(g) = 2CrO_3(g) \quad (3)$$

and/or

$$Cr_2O_3(s) + \frac{3}{2}O_2(g) + 2H_2O(g) = 2CrO_2(OH)_2(g) \quad (4)$$

The resulting chromia volatilization rates are excessive at high temperatures in flowing gases [2, 3, 5, 40, 41]. Whereas chromia alone provides a scale which is inadequate for high temperature service, in combination with a prior alumina layer it serves to extend alloy section lifetime substantially. It is desirable to be able to predict the duration of this extension.

As seen in Fig. 7, alloy chromium levels remain relatively high at the end of the longest exposure of 600 h at 1,200 °C. Nonetheless, localized breakaway had by then become evident at specimen corners (Fig. 15). Examination of one such breakaway site (Fig. 16) shows that the alumina layer had been breached, and extensive formation of $NiCr_2O_4$ had resulted. This oxide is much less stable than $NiAl_2O_4$ [42], and its formation indicates that an increase in oxygen potential had accompanied loss of the alumina barrier.

The breakaway at the specimen corners during exposure at 1,200 °C was first observed after 300 h exposure, i.e. when the Al content in the bulk specimen was virtually completely exhausted. Apparently, the complete exhaustion results at the specimen corners in formation of rapidly growing mixed oxides rather than subscale chromia formation observed on the flat areas of the specimen.

Although the onset of breakaway at specimen corners is accelerated by mechanical damage to the alumina layer because of out of plane tensile stresses [43], the alumina layer is also being consumed on flat specimen surfaces, as seen

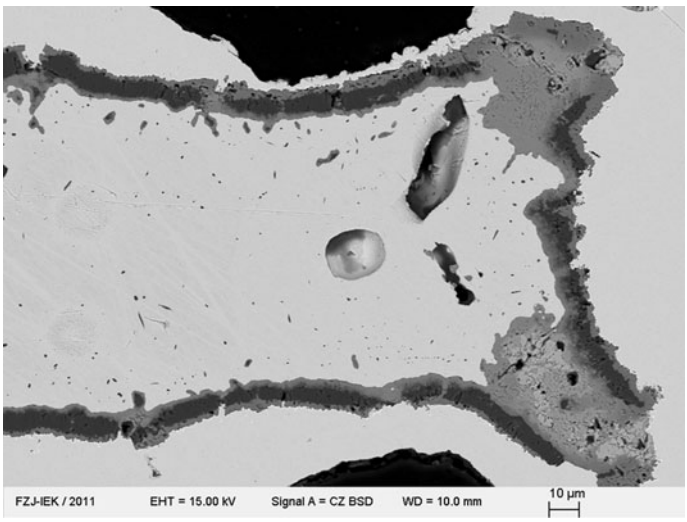

Fig. 15 Breakaway at specimen corners after 500 h oxidation at 1,200 °C

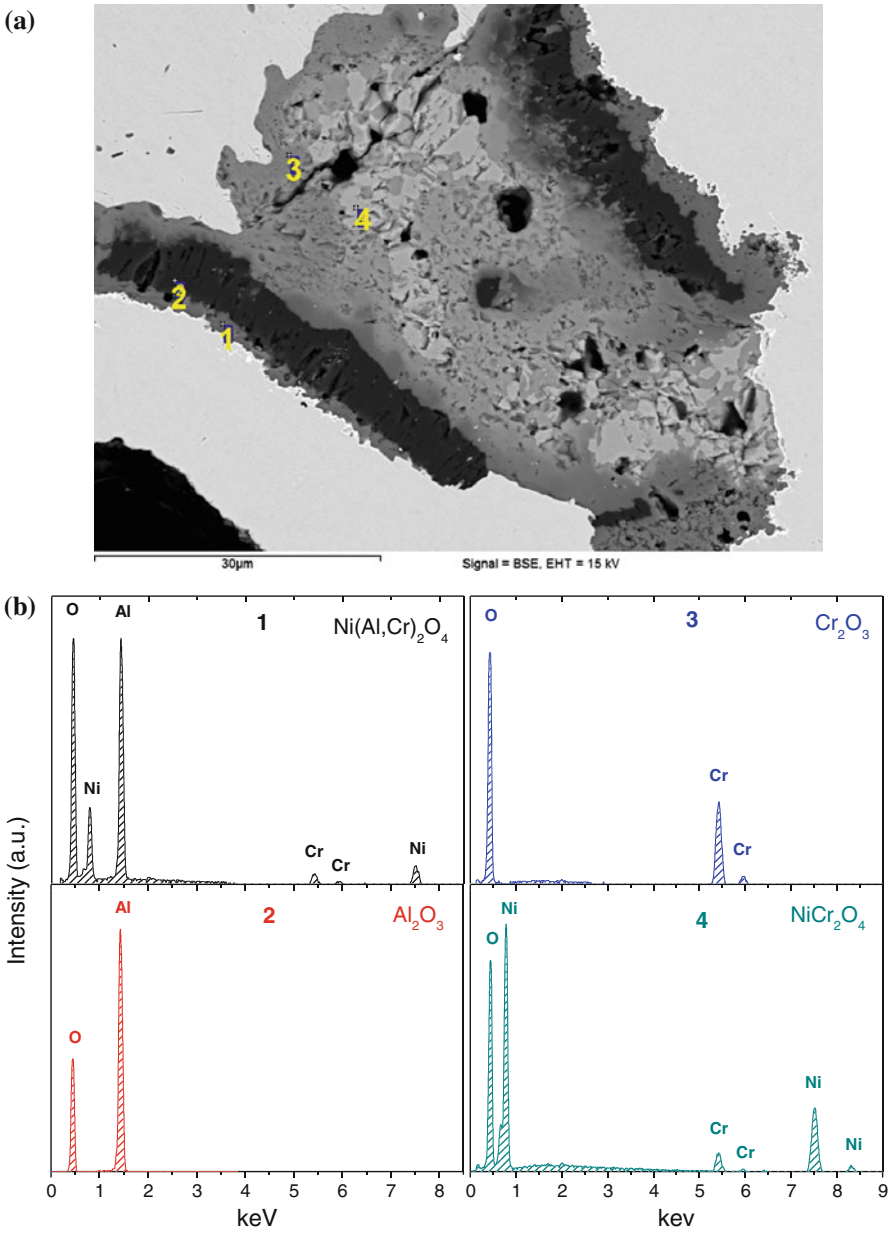

Fig. 16 Oxide morphology (**a**) and EDX spectra (**b**) of scale constituents after breakaway occurrence at specimen corner after 500 h oxidation at 1,200 °C

in Fig. 9b. Two processes are involved: dissolution of alumina into the slow growing chromia layer, and conversion to Ni-rich spinel at the spinel–alumina interface.

At temperatures above 900 °C, the miscibility of Al_2O_3 and Cr_2O_3 is complete [34, 44]. It is clear from the analysis results in Table 2 that aluminum dissolved in the chromia, but no evidence for bulk diffusion of Cr into the alumina was found.

It is apparent from the micrograph of Fig. 12 that attack on the alumina layer is most rapid at its grain boundaries. The columnar grain structure facilitates penetration, and this may be more important to layer breakdown than a uniform dissolution process. In this event, predicting the life expectancy of the alumina layer becomes difficult.

The rather slow growth of the outer Ni-rich spinel layer (Fig. 9) after complete exhaustion of the aluminium reservoir in the alloy is also at the expense of the alumina scale. For the reaction

$$\mathrm{Ni} + \mathrm{Al_2O_3(s)} + \frac{1}{2}\mathrm{O_2(g)} = \mathrm{NiAl_2O_4(s)} \tag{5}$$

(for which $\Delta G^\circ = -242100 - 74.6\ \mathrm{T\ J\ mol^{-1}}$) to occur, nickel must diffuse from the underlying alloy through both the chromia and alumina layers. Traces of nickel were detected in the chromia by EDS (Table 2), but not in the alumina. However, the SNMS profiles in Fig. 11b confirm penetration of nickel into the alumina after breakaway. It seems likely that nickel diffusion in Al_2O_3 is, like that of aluminum and oxygen at these temperatures, a grain boundary process [45]. Overall concentrations of nickel in the alumina layer would in this case be small.

Underlying chromia growth and outward nickel and chromium diffusion (to grow the outermost spinel layer) are in operation after the alloy aluminum content is exhausted, but not before. Both phenomena result from changes in oxygen and metal activities which follow the cessation of alumina layer growth. Measured alloy average compositions (Fig. 6) were used to calculate component activities from ThermoCalc [46] as a function of reaction time. Because the observed concentration profiles in the alloy are flat (Figs. 5, 7), these averages are taken to apply at the scale-alloy interface. As seen in Fig. 17, nickel activity at 1,200 °C steadily increases, as chromium activity decreases. Aluminum activity decreases over the first 300 h of oxidation, then drops sharply as the alloy component is exhausted. Subsequent residual levels cannot be measured, but are calculated from the equilibrium

$$2\underline{\mathrm{Cr}} + \mathrm{Al_2O_3} = 2\underline{\mathrm{Al}} + \mathrm{Cr_2O_3} \tag{6}$$

where underlining denotes an alloy solute species, using the value of a_{Cr} shown in Fig. 17. As the alloy aluminum content is reduced to this level, the ratio a_{Ni}/a_{Al} changes from 2×10^5 to 3×10^{14}. Simultaneously, the oxygen activity beneath the alumina layer rises from the value of 8×10^{-24} controlled by the equilibrium

$$2\underline{\mathrm{Al}} + \frac{3}{2}O_2 = \mathrm{Al_2O_3} \tag{7}$$

to the higher value of 9×10^{-18} set by the new scale-alloy equilibrium

$$2\underline{\mathrm{Cr}} + \frac{3}{2}\mathrm{O_2} = \mathrm{Cr_2O_3} \tag{8}$$

It is concluded therefore that the remnant alumina layer transmits oxygen, allowing chromia to form. The mechanism is presumably one of grain boundary

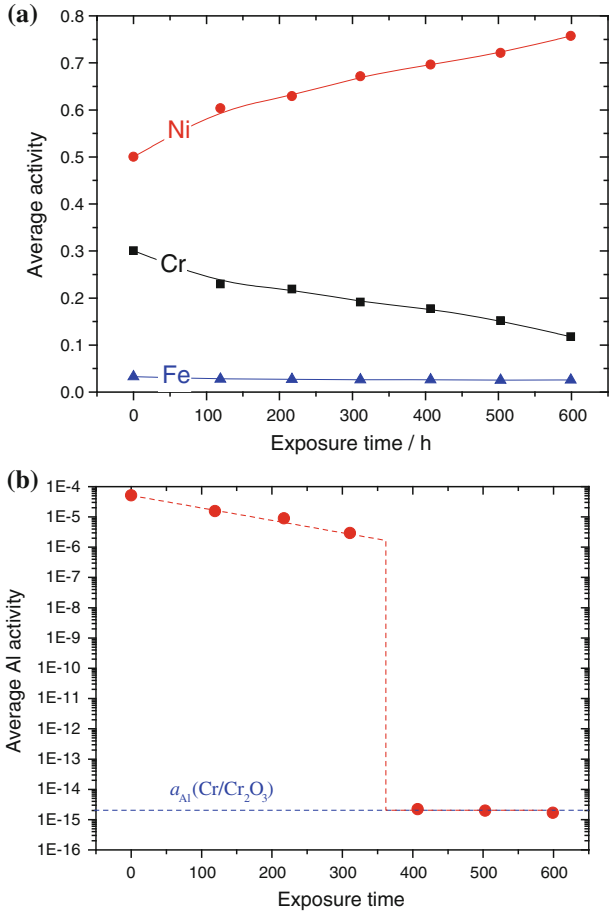

Fig. 17 Activities of alloy components (calculated in ThermoCalc [33, 46]) as a function of reaction time during oxidation at 1,200 °C. Data were calculated using alloy composition given in Fig. 6c

diffusion [47]. The unusually slow growth rate of the resulting chromia subscale results from limited oxygen availability beneath the alumina layer.

Overall diffusion of nickel through both chromia and alumina layers is driven by the gradients of both nickel and oxygen activities. It seems likely that the increase in a_O within the alumina layer accompanying the onset of chromia growth accounts for the effective increase in Al_2O_3 nickel permeability. Further spinel growth at the alumina-spinel interface via Eq. (5) then becomes possible.

Chromium Evaporation

Reactions (3) and (4) are not limited to pure chromia surfaces. Chromium-containing oxide phases like Ni- and/or Al-rich spinels release chromium at high temperatures in flowing gas by formation of $CrO_3(g)$ [48] (if no water vapour is present). The chemical

composition of the spinel layer in Fig. 2b measured by EDS indicates minor amounts of dissolved Cr, and should therefore be designated as $Ni(Cr,Al)_2O_4$. Figure 18 shows the measured evolution of the Cr and Al concentrations in the outer spinel layer during oxidation at 1,100–1,200 °C. At the lowest oxidation temperature of 1,100 °C, the Cr concentration in the spinel decreases gradually from 11 at% to virtually zero after 1,000 h. Simultaneously, the Al concentration rises from 17 to 27 at% at constant Ni concentration, clearly indicating that chromium in the spinel is being substituted by aluminium from the underlying layer by the reaction

$$Ni(Al_{1-x}Cr_x)_2O_4(s) + xAl_2O_3(s) + \frac{3}{2}xO_2(g) = NiAl_2O_4(s) + 2xCrO_3(g) \qquad (9)$$

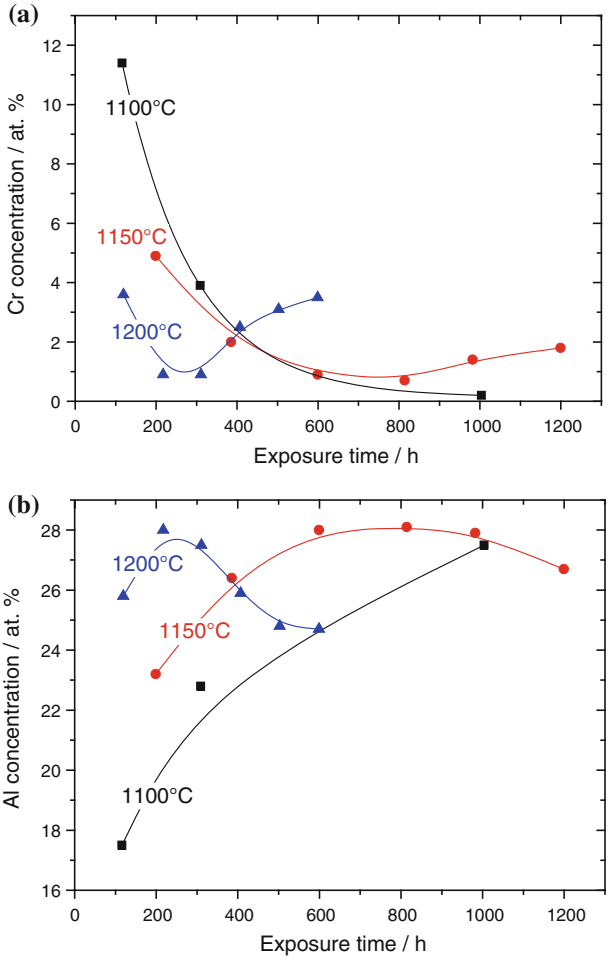

Fig. 18 Concentrations of Cr (**a**) and Al (**b**) in the outer spinel layer as a function of oxidation time at different temperatures (measured by EDS)

It is very likely that the decreasing Cr/Al-ratio in the spinel in the early time period is related to formation of volatile Cr-species according to Reaction (9). This loss in chromium may in fact result in a thinning of the spinel layer, which is, however, not clearly experimentally observed (Fig. 3).

Interesting in this context is the presence of substantial porosity in the spinel (Fig. 2a). The time and temperature dependence of this porosity was difficult to quantify but it seems not unlikely that void formation is affected by Cr-volatilization. Pint et al. [22] found more voids in the outer spinel layer grown on Haynes 214 in wet air at 1,100 °C than when reacted with laboratory air. Additionally, porosity is known to originate from reaction between various oxides in the transient oxidation stage [24, 28, 49].

After prolonged air exposure, the outer spinel layer is thus expected to consist exclusively of $NiAl_2O_4$ as found during 1,100 °C exposure. Qualitatively similar behavior is observed within the first 800 h of oxidation at 1,150 °C and in the first 300 h at 1,200 °C (Fig. 18). However, the Cr concentration in the spinel is seen in Fig. 18 to increase again after 800 h at 1,150 °C, and after approximately 300 h exposure at 1,200 °C. A matching decrease in Al concentration occurs simultaneously, whereas the nickel concentration remains constant and the spinel layer thickens. It should be mentioned that the relative error of the EDS analysis in Fig. 18 was approximately 10 %, i.e. the minimum of Cr concentration e.g. at 1,150 °C may seem doubtful as the variation of the values may fall within the measurement error. However, the reproducibility of the EDS analysis was very high for all specimens which at least confirms the qualitative shapes of the curves plotted in Fig. 18 although the given absolute concentration values may contain a systematic error.

A decrease in Cr level in the spinel layer with increasing time is also confirmed independently by the SNMS profiles (Fig. 11) after 1,150 °C oxidation.

The increase in chromium content of the spinel is obviously correlated with the formation of a $(Cr,Al)_2O_3$ layer beneath the alumina scale once the Al reservoir in the specimen is exhausted. As the alumina layer loses its protective properties, chromium starts to diffuse outwards to be incorporated into the spinel. The driving force for outward diffusion of chromium to the outer spinel layer is, of course, provided by the activity gradients in oxygen and chromium. What changes after longer exposure times is the increase in oxygen potential within and beneath the alumina layer as a result of the complete removal of Al from the underlying alloy. Evidently, this increases the solubility and/or mobility of chromium within the alumina, allowing its passage through the layer. At the same time, the alumina layer continues to shrink by interaction with the underlying chromia. Eventually, the scale should become duplex consisting of an outer $Ni(Cr,Al)_2O_4$ spinel layer and an inner mixed oxide $(Cr,Al)_2O_3$. At this point, the alloy would behave simply as a chromia-former, and lose utility at such high temperatures.

Summary and Concluding Remarks

Thin foils of Haynes 214 alloy have been oxidized in air at 1,100–1,200 °C. In the protective stage of oxidation, a duplex scale morphology was observed. An outer

$Ni(Al,Cr)_2O_4$ spinel layer grows readily in the first few hours of reaction, and remains intact while a protective alumina layer thickens beneath it.

Continued selective oxidation of Al from the thin foil results after a certain time in complete depletion of aluminum in the specimen. At this point, the alloy matrix can no longer maintain equilibrium with the Al_2O_3 scale, the oxygen potential beneath the alumina rises, and Cr_2O_3 formation at the alloy-scale interface commences. The resulting chromia layer grows beneath alumina at a remarkably slow rate. Its development serves to lengthen the alloy section lifetime by preventing immediate catastrophic oxidation after complete exhaustion of the alloy Al reservoir.

The outer $Ni(Al,Cr)_2O_4$ spinel formed during the transient oxidation stage becomes depleted in chromium due to evaporation of volatile chromium species. When the underlying alumina stops growing as a result of complete Al depletion, it becomes permeable to nickel, allowing further spinel growth and partial dissolution of Al_2O_3. More seriously, the newly formed chromia subscale dissolves the alumina layer from beneath. Eventually, the scale becomes one of mixed spinel $Ni(Al,Cr)_2O_4$ overlying $(Cr,Al)_2O_3$, and is no longer protective at these high temperatures.

Acknowledgments Mr. Cosler and Ms. A. Kick are kindly acknowledged for carrying out high temperature exposures and TG-analyses, Mr. M. Ziegner for XRD measurements, Mr. J. Bartsch and Mr. V. Gutzeit for metallographic preparation. The authors are grateful to Mr. M. Borzikov for carrying out SNMS analyses.

References

1. D. J. Young, *High Temperature Oxidation and Corrosion of Metals*, (Elsevier, Oxford, 2008).
2. C. Gindorf, L. Singheiser, and K. Hilpert, *Steel Research* **72**, 528 (2001).
3. W. J. Quadakkers, J. Piron-Abellan, V. Shemet, and L. Singheiser, *Materials at High Temperatures* **20**, 115 (2003).
4. J. Froitzheim, H. Ravash, E. Larsson, L. G. Johansson, and J. E. Svensson, *Journal of the Electrochemical Society* **157**, B1295 (2010).
5. D. J. Young and B. A. Pint, *Oxidation of Metals* **66**, 137 (2006).
6. D. Naumenko, V. Shemet, L. Singheiser, and W. J. Quadakkers, *Journal of Materials Science* **44**, 1687 (2009).
7. C. T. Sims, N. S. Stoloff, and W. C. Hagel, *Superalloys II—High Temperature Materials for Aerospace and Industrial Power* (Wiley, New York, 1987).
8. M. Bensch, J. Preussner, R. Huttner, G. Obigodi, S. Virtanen, J. Gabel, and U. Glatzel, *Acta Materialia* **58**, 1607 (2010).
9. R. Janakiraman, G. H. Meier, and F. S. Pettit, *Metallurgical and Materials Transactions A* **30**, 2905 (1999).
10. V. P. Deodeshmukh, S. J. Matthews, and D. L. Klarstrom, *International Journal of Hydrogen Energy* **36**, 4580 (2011).
11. B. A. Pint, L. R. Walker, and I. G. Wright, *Materials at High Temperatures* **21**, 175 (2004).
12. I. E. Anderson, B. K. Lograsso, R. Terpstra, and B. Gleeson, in *Powder Metallurgy Alloys and Particulate Materials for Industrial Applications*, eds., D. E. Alman and J. W. Newkirk (TMS, Warrandale, 2000), p. 11.
13. H. P. Degischer and B. Kriszt, *Handbook of Cellular Metals: Production, Processing Applications* (Wiley-VCH, Weinheim, 2002).
14. W. J. Quadakkers and K. Bongartz, *Werkstoffe und Korrosion* **45**, 232 (1994).
15. D. Naumenko, L. Singheiser, and W. J. Quadakkers, in *Cyclic Oxidation of High Temperature Materials* (EFC Publications, Frankfurt, 1999), p. 287.
16. H. E. Evans, A. T. Donaldson, and T. C. Gilmour, *Oxidation of Metals* **52**, 379 (1999).

17. W. J. Quadakkers and M. J. Bennett, *Materials Science and Technology* **10**, 126 (1994).
18. V. P. Deodeshmukh and S. K. Srivastava, in *Superalloys 2008* (Seven Springs, PA, 2008), p. 689.
19. D. J. Young, A. Chyrkin, and W. J. Quadakkers, *Oxidation of Metals* **77**, 253 (2012).
20. W. J. Quadakkers, A. Elschner, W. Speier, and H. Nickel, *Applied Surface Science* **52**, 271 (1991).
21. W. J. Quadakkers and H. Viefhaus, in *EFC-Workshop "Methods and Testing in High Temperature Corrosion"*, eds., H. J. Grabke and D. B. Meadowcroft (The Institute of Materials, Frankfurt, 1995).
22. B. A. Pint, R. W. Swindeman, K. L. More, and P. F. Tortorelli, ASME Paper 2001-GT-445, presented at the International Gas Turbine Aeroengine Congress Exhibition, New Orleans, LA, June 4–7 (2001).
23. C. S. Giggins and F. S. Pettit, *Journal of the Electrochemical Society* **118**, 1782 (1971).
24. L. Hu, D. B. Hovis, and A. H. Heuer, *Oxidation of Metals* **73**, 275 (2010).
25. B. H. Kear, F. S. Pettit, L. P. Lemaire, and D. E. Fornwalt, *Oxidation of Metals* **3**, 557 (1971).
26. G. C. Wood and B. Chattopa, *Corrosion Science* **10**, 471 (1970).
27. G. C. Wood, B. Chattopa, and F. H. Stott, *Journal of the Electrochemical Society* **117**, 254 (1970).
28. M. C. Maris-Sida, G. H. Meier, and F. S. Pettit, *Metallurgical and Materials Transactions A* **34**, 2609 (2003).
29. F. A. Elrefaie and W. W. Smeltzer, *Journal of the Electrochemical Society* **128**, 2237 (1981).
30. K. T. Jacob and C. B. Alcock, *Journal of Solid State Chemistry* **20**, 79 (1977).
31. A. Borgenstam, A. Engstrom, L. Hoglund, and J. Agren, *Journal of Phase Equilibria* **21**, 269 (2000).
32. MOBNi1, *TCS Ni-Alloys Mobility Database* (Royal Institute of Technology, Foundation of Computational Thermodynamics, Stockholm, 2006).
33. TTNI7, *TT Ni-Based Superalloys Database* (Thermo-Calc Software AB, Stockholm, 2006).
34. F. Bondioli, A. M. Ferrari, C. Leonelli, T. Manfredini, L. Linati, and P. Mustarelli, *Journal of the American Ceramic Society* **83**, 2036 (2000).
35. G. J. Tatlock, H. Al-Badairy, M. J. Bennett, and J. R. Nicholls, *Materials at High Temperatures* **22**, 467 (2005).
36. G. Strehl, H. Al-Badairy, L. M. Rodriguez, J. Klower, G. Borchardt, G. Tatlock, and A. J. Criado, in *Cyclic Oxidation of High Temperature Materials: Mechanisms, Testing Methods, Characterisation and Life Time Estimation* (EFC Publications, Frankfurt, 1999), p. 82.
37. D. J. Potter and G. J. Tatlock, *High Temperature Corrosion and Protection of Materials* **7**(Pts 1 and 2) 1093 (2008).
38. H. E. Evans and M. P. Taylor, *Oxidation of Metals* **55**, 17 (2001).
39. D. Caplan and G. I. Sproule, *Oxidation of Metals* **9**, 459 (1975).
40. G. R. Holcomb, *Oxidation of Metals* **69**, 163 (2008).
41. H. Asteman, J. E. Svensson, L. G. Johansson, and M. Norell, *Oxidation of Metals* **52**, 95 (1999).
42. P. Saltykov, O. Fabrichnaya, J. Golczewski, and F. Aldinger, *Journal of Alloys and Compounds* **381**, 99 (2004).
43. M. Schütze, M. Malessa, D. Renusch, P. F. Tortorelli, I. G. Wright, and R. B. Dooley, in *High-Temperature Oxidation and Corrosion* (ISHOC 2005, Nara, Japan, 30 Nov–2 Dec 2006), p. 393.
44. K. T. Jacob, *Journal of the Electrochemical Society* **125**, 175 (1978).
45. K. P. Trumble and M. Rühle, *Acta Metall. Mater.* **39**, 1915 (1991).
46. B. Jansson, M. Schalin, M. Selleby, and B. Sundman, in *Computer Software in Chemical and Extractive Metallurgy*, eds., C. W. Bale and G. A. Irons (Canadian Inst Mining, Metallurgy and Petroleum, Montreal, 1993), p. 57.
47. W. J. Quadakkers, H. Holzbrecher, K. G. Briefs, and H. Beske, *Oxidation of Metals* **32**, 67 (1989).
48. B. Pujilaksono, T. Jonsson, H. Heidari, M. Halvarsson, J. E. Svensson, and L. G. Johansson, *Oxidation of Metals* **75**, 183 (2011).
49. W. G. Sloof and T. J. Nijdam, *International Journal of Materials Research* **100**, 1318 (2009).